nature neuroscience

Fluorescent false neurotransmitter reveals functionally silent dopamine vesicle clusters in the striatum

Daniela B Pereira[1,6], Yvonne Schmitz[1], József Mészáros[2], Paolomi Merchant[3], Gang Hu[3,6], Shu Li[3,6], Adam Henke[3,6], José E Lizardi-Ortiz[1], Richard J Karpowicz Jr[3,6], Travis J Morgenstern[4], Mark S Sonders[1,2], Ellen Kanter[1], Pamela C Rodriguez[3,6], Eugene V Mosharov[1], Dalibor Sames[3] & David Sulzer[1,2,4,5]

Neurotransmission at dopaminergic synapses has been studied with techniques that provide high temporal resolution, but cannot resolve individual synapses. To elucidate the spatial dynamics and heterogeneity of individual dopamine boutons, we developed fluorescent false neurotransmitter 200 (FFN200), a vesicular monoamine transporter 2 (VMAT2) substrate that selectively traces monoamine exocytosis in both neuronal cell culture and brain tissue. By monitoring electrically evoked Ca^{2+} transients with GCaMP3 and FFN200 release simultaneously, we found that only a small fraction of dopamine boutons that exhibited Ca^{2+} influx engaged in exocytosis, a result confirmed with activity-dependent loading of the endocytic probe FM1-43. Thus, only a low fraction of striatal dopamine axonal sites with uptake-competent VMAT2 vesicles are capable of transmitter release. This is consistent with the presence of functionally 'silent' dopamine vesicle clusters and represents, to the best of our knowledge, the first report suggestive of presynaptically silent neuromodulatory synapses.

Dopaminergic neurotransmission is important for habit formation, motor learning and reward-seeking behaviors, and abnormalities in dopamine transmission underlie important features of psychiatric and neurological disorders. Elucidating mechanisms that regulate dopamine release is essential for understanding normal and diseased brain function. Striatal dopamine exocytosis has been characterized with high chemical specificity by microdialysis[1] and high temporal resolution with carbon fiber cyclic voltammetry (CV) and amperometry[2,3]. Although these methods have greatly advanced our knowledge of dopaminergic neurotransmission, they integrate release and reuptake from hundreds of boutons and lack the ability to monitor the range of responses and spatial dynamics of transmitter release from individual synapses.

Electron microscopy studies have suggested morphological heterogeneity of striatal dopaminergic synapses, with a fraction of synaptic vesicle–containing axonal sites lacking synaptic membrane densities[4,5]. Little is known, however, about the functional range of dopaminergic 'presynaptic sites' in the striatum. Optical techniques provide the spatial resolution required to address these issues. Endocytic FM dyes[6] and the genetically encoded synaptopHluorins[7] have been used to study dopaminergic exocytosis in cultured neurons[8–11]. These probes, however, are not specific for dopamine boutons, and *post hoc* immunostaining is required to confirm dopaminergic identity, which is impractical when studying brain tissue. We recently introduced the fluorescent false neurotransmitters (FFNs) FFN511 and FFN102, fluorescent dopamine analogs that let us detect transmitter release from dopamine boutons in brain tissue[12,13]. These FFNs, however, possess intrinsic characteristics that complicate the accurate monitoring of destaining kinetics and do not successfully label dopaminergic synapses in cultured neurons.

We developed FFN200 as the first FFN to label dopaminergic neurons in both culture and the acute brain slice. We found that the majority of striatal FFN200-labeled axonal sites loaded the probe into VMAT2-containing vesicles and exhibited electrically evoked GCaMP3-monitored Ca^{2+} transients. Only a small fraction of these vesicle clusters, however, exhibited exocytosis in response to local electrical stimulation, which was independently confirmed by the well-characterized endocytic tracer FM1-43. Our results suggest that, in dopaminergic axons, the majority of vesicle clusters capable of accumulating neurotransmitter are functionally silent, as a result of a blockade of exocytosis at a step downstream from Ca^{2+} influx.

RESULTS

FFN200 selectively labels striatal dopamine axons

With the aim of developing optical probes to study monoamine exocytosis from individual boutons, we designed FFN200 as a fluorescent substrate of VMAT2 (**Fig. 1a**), the predominant isoform of the synaptic vesicle monoamine transporter in the CNS[14]. FFN200 was confirmed

[1]Department of Neurology, Columbia University Medical Center, New York, New York, USA. [2]Department of Psychiatry, Columbia University Medical Center, New York, New York, USA. [3]Department of Chemistry, Columbia University, New York, New York, USA. [4]Department of Pharmacology, Columbia University Medical Center, New York, New York, USA. [5]Department of Neuroscience, New York Psychiatric Institute, New York, New York, USA. [6]Present addresses: Champalimaud Neuroscience Programme, Champalimaud Centre for the Unknown, Lisbon, Portugal (D.B.P.), Infineum USA, Linden, New Jersey, USA (G.H.), Pharmasan Labs, Osceola, Wisconsin, USA (S.L.), California Institute for Biomedical Research, La Jolla, California, USA (A.H.), Department of Pathology and Laboratory Medicine, Center for Neurodegenerative Disease Research, Perelman School of Medicine, University of Pennsylvania, Pennsylvania, USA (R.J.K.), Institute of Biology, École Normale Supérieure, Paris, France (P.C.R.). Correspondence should be addressed to D.B.P. (nydp2003@gmail.com), D. Sames (ds584@columbia.edu) or D. Sulzer (ds43@cumc.columbia.edu).

Received 26 September 2015; accepted 15 January 2016; published online 22 February 2016; doi:10.1038/nn.4252

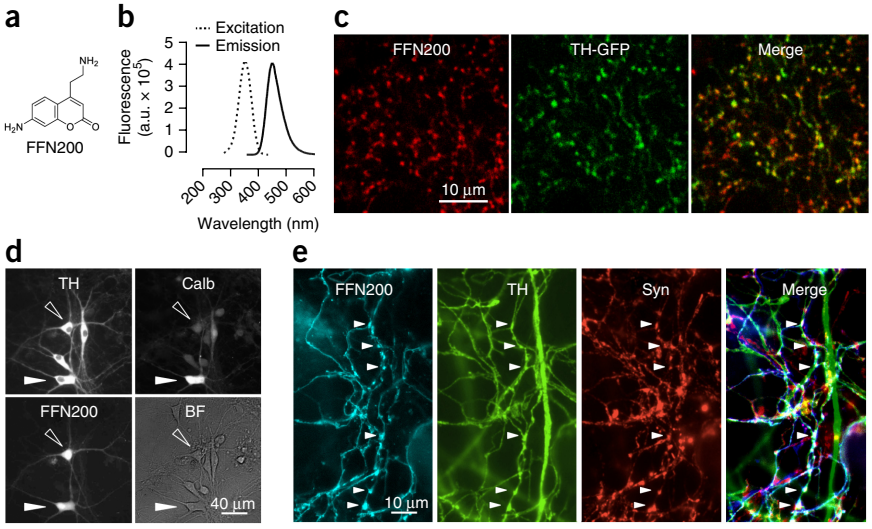

Figure 1 Structure, spectral properties and selectivity of FFN200. (**a**) Structure of FFN200. (**b**) Excitation and emission spectra of FFN200. (**c**) Representative images of FFN200-GFP colocalization. Striatal slices of TH-GFP mouse brains were loaded with FFN200 (10 µM, 30 min) and imaged sequentially for FFN200 and GFP. (**d**) Representative images of FFN200-labeled dopamine ventral midbrain neurons in culture subsequently immunolabeled for TH and calbindin (calb). Calbindin-negative and calbindin-positive FFN200-loaded neurons are indicated with empty and solid arrowheads, respectively. A bright field (BF) image is shown in which TH-negative neurons are also present. (**e**) Representative images of axonal fields in midbrain neuronal cultures labeled with FFN200, and immunostained for TH and synaptophysin (syn). Neurons were incubated with FFN200 and images were acquired shortly after fixative addition to minimize potential organelle movement. Solid arrowheads mark FFN200 puncta expressing both TH and synaptophysin.

as a VMAT2 substrate, as its accumulation in VMAT2-transfected HEK cells was inhibited by tetrabenazine (TBZ) and exhibited a K_m of 13.7 ± 2.7 µM (n = 3, Online Methods). The fluorescence excitation and emission maxima of FFN200 were determined to be 352 and 451 nm (**Fig. 1b**), respectively, allowing good spectral separation from most green and red fluorophores. The logD of FFN200, which indicates the probe's partition between octanol and pH 7.4 potassium phosphate buffer, was −1.29, indicating that FFN200 is a highly polar compound unlikely to diffuse across membranes.

Striatal brain slices incubated with FFN200 exhibited a punctate pattern of fluorescent labeling that was suggestive of synaptic bouton staining (**Fig. 1c**). To investigate the selectivity of FFN200 toward dopaminergic structures, we used striatal slices from mice expressing GFP under the tyrosine hydroxylase promoter (TH-GFP mice)[15]. In the striatum, GFP was expressed mostly in dopaminergic axons, the predominant monoaminergic input to this brain region[16,17]. The majority of FFN200 puncta colocalized with GFP (84.6 ± 2.6%, n = 5 slices from 5 mice; **Fig. 1c**), indicating that the probe is selective for striatal dopaminergic axonal profiles and ruling out a substantial fraction of serotonergic boutons.

Given that no monoamine-specific optical tracers have been identified that monitor exocytosis in cultured dopaminergic neurons, we analyzed FFN200 staining of TH-GFP ventral midbrain neuronal cultures. Approximately 70% of cultured dopamine neurons, identified by the presence of GFP, were found to accumulate FFN200 (**Supplementary Fig. 1**). Conversely, 100% of FFN200-positive cells were immunolabeled for TH after FFN200 imaging (immunolabeling for TH was performed, as not all cultured TH-positive neurons from TH-GFP mouse expressed GFP; **Fig. 1d**). These results indicate that FFN200 selectively labels ventral midbrain dopaminergic cell bodies in culture.

To determine whether there is differential accumulation of FFN200 between substantia nigra (SN) and ventral tegmental area (VTA) dopaminergic neurons, we double labeled midbrain neuronal cultures for TH and calbindin after FFN200 imaging (**Fig. 1d**). Calbindin is predominantly present in VTA and is absent in SN dopamine neurons[18]. In these cultures, 66% of TH-positive neurons expressed calbindin. FFN200-positive and FFN200-negative neurons exhibited comparable percentages of calbindin expression: 67% and 63%, respectively (40 cells, representative of two independent cell culture preparations). These results suggest that FFN200 does not discriminate between SN- and VTA-derived dopaminergic neurons in culture.

The distribution of FFN200 in cell bodies and dendrites of cultured neurons was diffuse, suggesting that, in addition to labeling VMAT2-containing organelles, a substantial fraction of the probe is located in the cytosol (**Fig. 1d**). In axonal regions of cultured neurons, FFN200 fluorescence was characterized by a clear punctate pattern, which is likely to be the correlate of striatal slice FFN200 puncta, superimposed on a lighter diffuse signal that filled the axonal cytosol (**Fig. 1e**). Triple colocalization between FFN200, TH and the synaptic vesicle protein synaptophysin revealed that 86 ± 6% of all TH-labeled FFN200 puncta expressed synaptophysin (total of 193 puncta from five cell culture preparations; **Fig. 1e**). The data indicate that most FFN200 puncta represent sites of synaptic vesicle accumulation in cultured dopaminergic neurons.

FFN200 accumulation in striatal axons depends on VMAT2

To understand the mechanism of FFN200 accumulation, we investigated the putative role of the plasma membrane and synaptic vesicle dopamine transporters. No difference was found in the number and intensity of FFN200 puncta in the dorsolateral striatum of mice lacking the *Slc6a3* gene, which encodes the DAT protein, and wild-type littermates using identical FFN200 loading protocols (number of puncta per field of view: wild type, 441.7 ± 35.2; DAT knockout (KO), 412.9 ± 33.4; n = 3 mice per condition with 2 slices averaged per mouse, P = 0.59, two-tailed unpaired t test; **Fig. 2a**,**b**). DAT inhibition with nomifensine had no significant effect on striatal FFN200 accumulation (number of puncta: wild type, 418.8 ± 20.5; nomifensine, 434.8 ± 20.5; n = 4 mice per condition with two slices averaged per mouse, P = 0.60, two-tailed unpaired t test; **Fig. 2a**,**b**). Moreover, FFN200 loading into cultured midbrain dopamine neurons was not impaired by either DAT KO (data not shown) or iso-osmotic replacement of Na^+ with choline (FFN200-labeled dopamine neurons: NaCl, 59.0 ± 12.0%; choline Cl, 60.0 ± 10.0%; n = 3 independent cell cultures, P = 0.95, two-tailed unpaired t test). Thus, FFN200, in contrast with FFN102 (ref. 13), does not rely on DAT or other Na^+-dependent transporters for loading into dopaminergic neurons.

FFN200 puncta intensity was reduced by approximately 30% in the dorsolateral striatum of VMAT2 hypomorph striatal slices, which

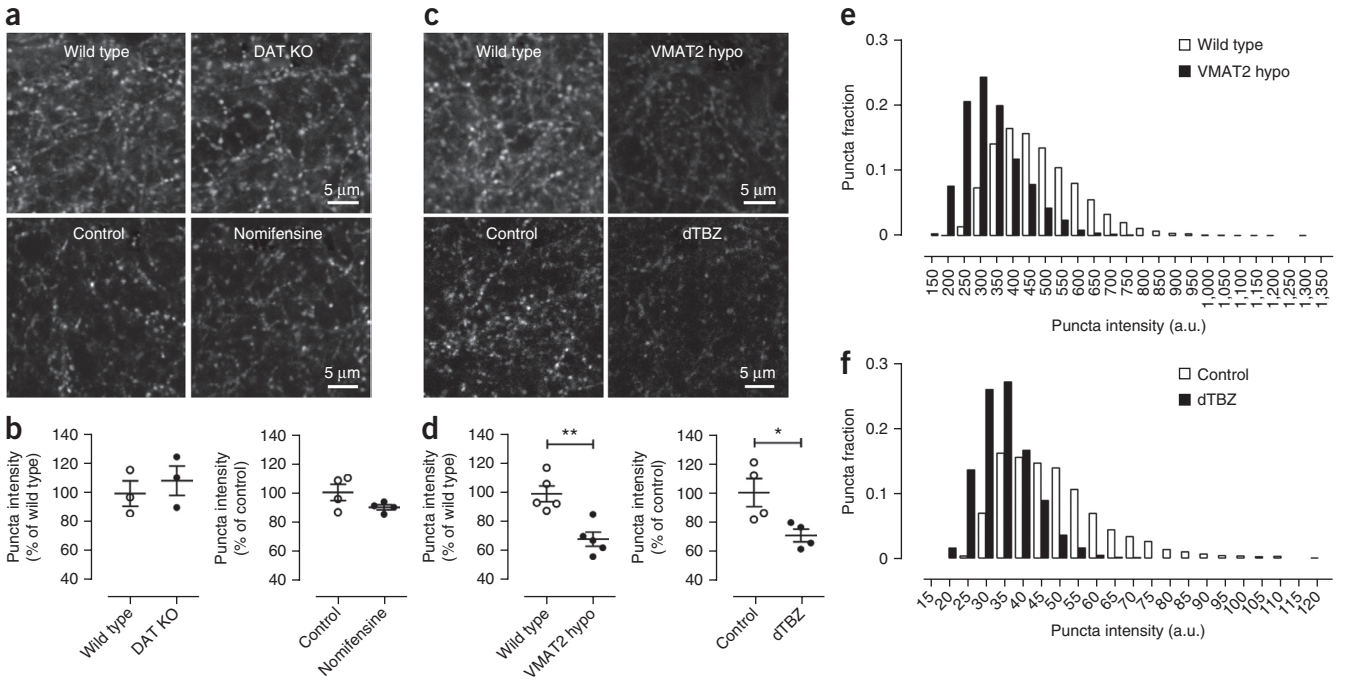

Figure 2 Effect of DAT and VMAT2 inhibition or genetic ablation on FFN200 loading in the dorsal striatum. (**a**,**c**) Representative images of FFN200-loaded striatal slices from wild-type and DAT KO (**a**) or VMAT2 hypomorph mice (VMAT2 hypo; **c**) (top panels) and of untreated control slices and slices treated with 5 µM nomifensine for 10 min before and during FFN200 incubation (**a**) or dTBZ-treated slices (5 µM dTBZ for 1 h before and during FFN200 loading; **c**) (bottom panels). (**b**,**d**) FFN200 puncta intensity in slices of versus DAT KO mice ($n = 3$) and in control versus nomifensine-treated slices ($n = 4$) (**b**), and in slices from wild-type versus VMAT2 hypomorph mice ($n = 5$) and in control versus dTBZ-treated slices ($n = 4$) (**d**). Puncta intensities were background-subtracted and normalized to the corresponding mean wild-type or control value and are plotted as a scatter plot including mean ± s.e.m. ($n = 3$–5 mice, as indicated above, with two slices averaged per mouse) with significant differences indicated (two-tailed unpaired t test, $^*P < 0.05$, $^{**}P < 0.01$; wild-type versus DAT KO, $P = 0.54$; control versus nomifensine, $P = 0.13$; wild-type versus VMAT2 hypomorph, $P = 0.0027$; control versus dTBZ, $P = 0.031$). (**e**,**f**) Histograms of puncta intensities, in arbitrary units (a.u.), for all FFN200 puncta of wild-type versus VMAT2 hypomorph (**e**) and control versus dTBZ-treated slices (**f**).

express ~5% of wild-type VMAT2 protein levels[19,20] (**Fig. 2c**,**d**). A similar reduction in puncta intensity was observed following treatment with the VMAT2 inhibitor dihydrotetrabenazine (dTBZ) under conditions that led to maximal VMAT2 inhibition, as assessed by measuring evoked dopamine release with CV (**Fig. 2c**,**d** and **Supplementary Fig. 2**). The entire distribution of FFN200 puncta intensities was shifted to lower values in both VMAT2 hypomorph and dTBZ-treated slices (**Fig. 2e**,**f**), indicating that the majority of FFN200 puncta had lower intensity when VMAT2 activity was decreased. The number of FFN200 puncta was also reduced by dTBZ (control, 351.5 ± 9.8 puncta; dTBZ, 249.0 ± 2.9; $n = 4$ mice with 2 slices averaged per mouse, $P < 0.0001$, two-tailed unpaired t test) and in the VMAT2 hypomorphs (wild type, 378.7 ± 4.8 puncta; VMAT2 hypomorph, 265.5 ± 2.3; $n = 5$ mice with 2 slices averaged per mouse, $P < 0.0001$, two-tailed unpaired t test), which suggests that some puncta fell below the detection threshold as a result of decreased intensity. These data suggest that FFN200 loading in striatal slices is in part dependent on VMAT2, the majority of puncta have FFN200 in VMAT2-containing vesicles and ~30% of the total FFN200 in each punctum is located in VMAT2 vesicles.

FFN200 activity–induced release is strictly VMAT2 dependent

Time lapse imaging of FFN200 puncta in striatal slices revealed that FFN200 was released into the extracellular space following perfusion with 40 mM KCl-containing buffer (**Fig. 3a**), as measured by the increase in background intensity, that is, the average fluorescence intensity in non-punctal regions (given that high K^+ depolarization caused considerable tissue distortion, we did not analyze FFN200 destaining from individual puncta; **Fig. 3b**). KCl depolarization also induced FFN200 release in midbrain dopamine neurons in culture (**Fig. 3c**,**d**), confirming that the probe can be used to monitor dopamine exocytosis in cultured neurons. Notably, although most FFN200 puncta in cultured neurons colocalized with synaptophysin (86%; **Fig. 1e**), a subset did not destain in response to KCl (**Fig. 3c**). Moreover, substantial axonal FFN200 fluorescence remained, which is consistent with cytoplasmic localization of a fraction of FFN200 (**Fig. 1d**).

High K^+ depolarization did not significantly destain FFN200 in VMAT2 hypomorph striatal slices, as indicated by the lack of change in background fluorescence intensity ($P < 0.0001$, two-way ANOVA; **Fig. 3a**,**b**). These results indicate that the majority of activity-induced FFN200 release in the striatum originates from VMAT2-expressing vesicles and that the remaining fluorescence of FFN200 puncta in VMAT2 hypomorphs is located in the cytoplasm or organelles that do not undergo stimulus-dependent exocytosis.

FFN200 provides monitoring of individual bouton exocytosis

Local electrical stimulation of striatal axons at 15 Hz, a frequency associated with dopamine neuron burst firing[21], induced destaining of a subset of FFN200 puncta (**Fig. 4a**). Representative time-lapse images and destaining curves for individual puncta showed a range of destaining kinetics (**Fig. 4a**,**b**). Some puncta did not respond to stimulation and were indistinguishable from those in non-stimulated slices (**Fig. 4a**,**b**). FFN200 release into the extracellular

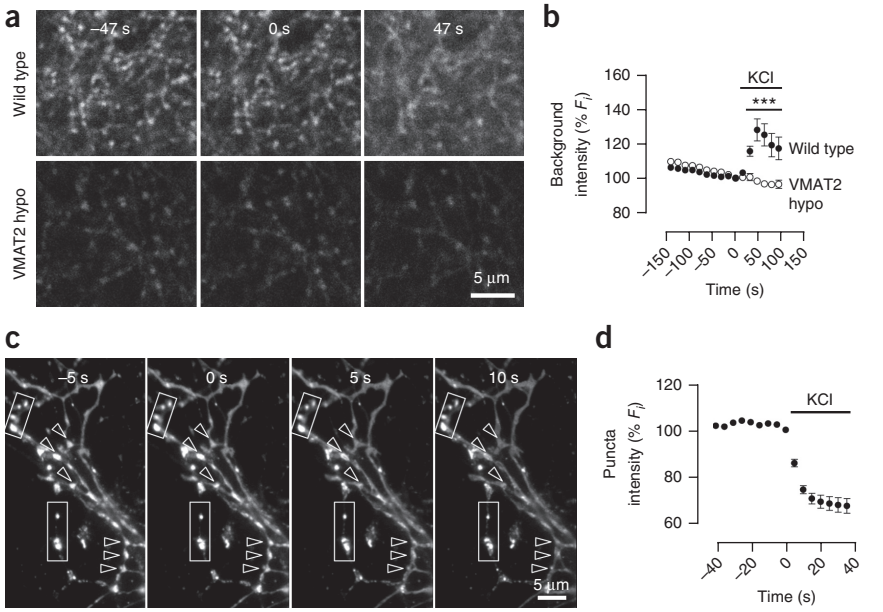

Figure 3 KCl-induced destaining of FFN200 in striatal slices and ventral midbrain cell cultures. (**a**) Representative images at the three indicated time points of KCl-induced FFN200 destaining experiments in wild-type and VMAT2 hypomorph (VMAT2 hypo) dorsal striatum. Time 0 s represents the final image before high K^+ stimulation. (**b**) Quantification of background fluorescence intensity, showing KCl-induced release of FFN200. Data are normalized to the intensity value at time point zero (F_i) and presented as mean percentage of $F_i \pm$ s.e.m. ($n = 5$ mice per genotype with 1–2 slices averaged per mouse). Wild-type and VMAT2 hypomorph curves were significantly different ($P < 0.0001$, two-way ANOVA) as was the effect of KCl over time ($P < 0.0001$) and the interaction between genotype and KCl ($P < 0.0001$). The wild-type and VMAT2 hypomorph curves were also significantly different at the indicated time points (Bonferroni post test, $^{***}P < 0.001$). (**c**) Representative images of KCl (90 mM)-evoked release of FFN200 in cultured midbrain neurons. Examples of destaining and non-destaining puncta are indicated with arrowheads and rectangles, respectively. (**d**) Intensity versus time plot for FFN200 puncta that destained by at least 20% in response to high K^+ in cultured midbrain neurons. Data is presented as mean percentage of $F_i \pm$ s.e.m. ($n = 6$ different cell cultures).

milieu was confirmed by measuring the increase in background intensity following stimulation (**Fig. 4c**). This activity-induced release of FFN200 was Ca^{2+} dependent, as the background intensity failed to increase in slices stimulated in the presence of the Ca^{2+} channel blocker $CdCl_2$ (200 µM; **Fig. 4c**) or in 0 mM Ca^{2+} buffer (**Supplementary Fig. 3a**). Consistently, changes in the intensity of FFN200 puncta in slices stimulated in the presence of Cd^{2+} were indistinguishable from those of unstimulated slices (**Fig. 4a**,**b**). Stimulation-evoked FFN200 destaining was blocked by 1 µM tetrodotoxin (TTX; **Supplementary Fig. 3a**). The results indicate a requirement for action potential conduction through axonal processes to evoke FFN200 release, similar to results from CV recordings of evoked dopamine release[3].

To reliably analyze the FFN200 puncta that destain following stimulation, we developed a Matlab program to discriminate destaining from non-destaining puncta in a consistent and unbiased manner (Online Methods). We obtained a percentage of 'destaining' puncta of 4.0 ± 0.9%, 2.9 ± 0.6%, 4.7 ± 1.3% and 3.3 ± 1.1% for unstimulated slices and slices stimulated in the presence of Cd^{2+} or TTX or in 0 mM Ca^{2+}, respectively (**Fig. 4d** and **Supplementary Fig. 3b**), which represent the rate of false positives obtained with this method. The percentage of destaining puncta for 15-Hz stimulated slices was significantly higher at 17.2 ± 2.0% ($P < 0.001$, one-way ANOVA with Bonferroni's multiple comparison test; **Fig. 4d**).

We examined the change in FFN200 puncta intensity over time, corrected for the baseline rundown, for destaining and non-destaining puncta (**Fig. 4e**). There was an average of 28% evoked decrease in fluorescence per destaining punctum, consistent with the VMAT2 hypomorph and dTBZ data suggesting that ~30% of each punctum's fluorescence is present in VMAT2-containing compartments (**Fig. 2b**,**d**). As evident from the first derivative of the destaining curve (**Fig. 4f**), the loss in FFN200 intensity was greatest at the onset of stimulation and decreased thereafter. Individual destaining curves were fit by monoexponential decay functions and the distribution of destaining halftimes ($t_{1/2s}$) was plotted (**Fig. 4g**). The average of the median $t_{1/2}$ values obtained for each slice was 25.7 ± 2.5 s. Comparing FFN200 and FFN102 destaining at 15 Hz revealed slower destaining kinetics for FFN102 (**Supplementary Fig. 4c**,**d**). This may be a result of the pH dependence of FFN102 fluorescence, which, for example, complicates adequate background subtraction (we found a greater increase in FFN102 background fluorescence without a significant increase in the fraction of destaining puncta as a result of the increased FFN102 intensity at neutral pH at $\lambda_{exc} = 770$ nm; $P = 0.1269$, two-tailed unpaired t test; **Supplementary Fig. 4a**,**b**)[13]. The pH-independent fluorescence of FFN200 makes this probe a better indicator of neurotransmitter release kinetics.

We monitored FFN200 destaining at a range of stimulation frequencies and found that, although the percentage of destaining puncta did not change significantly ($P = 0.1039$ by one-way ANOVA; **Fig. 5a**), destaining kinetics became faster with increased frequency, as expected (**Fig. 5b**,**c**). Plotting the decrease of puncta intensity as a function of stimulation pulse number revealed that the amount of FFN200 released per pulse decreased as stimulation frequency increased (**Fig. 5d**), consistent with electrochemically recorded dopamine release in striatal brain slices[22,23]. The $t_{1/2}$ of FFN200 release was reached at 318, 135, 41 and 5 stimulation pulses at 15, 4, 1 and 0.1 Hz, respectively. Moreover, ~17% of FFN200-labeled vesicles in the releasable pool underwent exocytosis in response to a single stimulus pulse (compare first stimulus at 0.1 Hz (4.7% decrease) to maximal release (28.5%); **Fig. 5d**,**e**), consistent with the high levels of dopamine release elicited by individual pulses[22,23]. Thus, FFN200 release triggered by a single stimulus can be measured with this approach.

FFN200 and FM1-43 reveal silent dopamine vesicle clusters

The percentage of FFN200 puncta that destained in response to 15 Hz stimulation was 17.2 ± 2.0% (**Fig. 4d**). The density of striatal FFN200 puncta was found to be 0.126 ± 0.009 puncta μm^{-3} (determined in maximal projections of stacks of five z sections, acquired 0.5 µm apart; $n = 5$ slices from different mice), similar to the density of striatal dopamine synapses previously reported by serial section electron microscopy (~0.1 synapses μm^{-3}; dopamine synapses were defined as a cluster of vesicles in close proximity to symmetric membrane densities in 5-OHDA–labeled axons)[24,25].

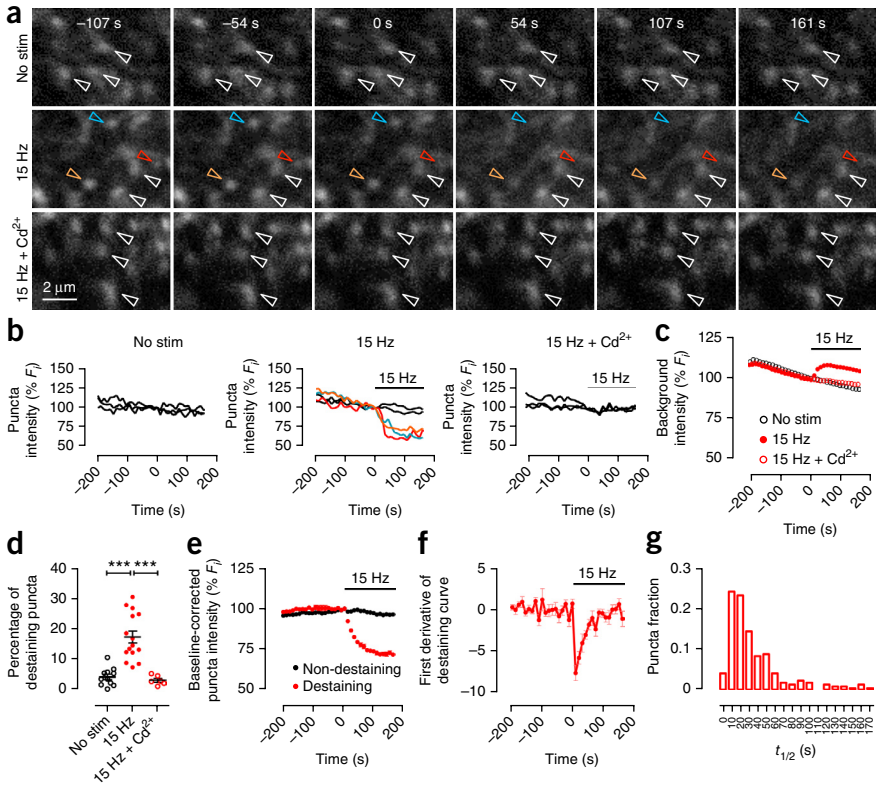

Figure 4 Electrically evoked FFN200 release in striatal slices. (**a**) Representative images of dorsal striatum of unstimulated slices (no stim) and slices stimulated at 15 Hz in the absence (15 Hz) or presence of 200 µM $CdCl_2$ (15 Hz + Cd^{2+}). Time 0 s represents the final image before stimulation. Colored and white arrowheads exemplify destaining and non-destaining puncta, respectively. (**b**) Representative intensity versus time traces of the individual puncta indicated by arrowheads in **a**, background-subtracted and normalized to the intensity value at 0 s (F_i). Arrowheads and intensity traces of similar color were used for each destaining punctum. (**c**) Background intensity presented as mean percentage of $F_i \pm$ s.e.m. ($n = 6$ for 15 Hz + Cd^{2+}, $n = 11$ for No stim and $n = 15$ for 15 Hz, where n is number of mice, with 1–2 slices averaged per mouse). (**d**) Scatter plot of the percentage of destaining puncta in each independent experiment including mean ± s.e.m. (n as in **c**; $^{***}P < 0.001$, one-way ANOVA with Bonferroni's multiple comparison test). (**e**) Mean background-subtracted puncta intensity over time for destaining and non-destaining puncta in stimulated slices, corrected for baseline fluorescence rundown (mean percentage of $F_i \pm$ s.e.m., $n = 15$ slices from different mice). (**f**) First derivative of the baseline-corrected intensity versus time curve for destaining puncta shown in **e**. Error bars represent ±s.e.m. (**g**) Histogram of destaining halftimes ($t_{1/2}$) for all destaining puncta (216 puncta from 15 slices from different mice). Error bars are included in all plots, but in some cases are occluded by the symbols.

The low fraction of destaining puncta is therefore unlikely to represent axonal regions that lack synaptic vesicles, as the density of FFN200 puncta would otherwise be considerably higher. Furthermore, the shift of the entire distribution of FFN200 puncta intensities to lower values in VMAT2 knockdown and inhibition experiments (**Fig. 2e**,**f**) indicates that the majority of FFN200 puncta contain the probe in VMAT2-expressing vesicles.

Putative leakage of FFN200 from synaptic vesicles or depletion of vesicular FFN200 by spontaneous vesicle fusion could in principle occur during the 45-min wash time chosen for optimal signal selectivity. Decreasing the washout to 25 min, however, did not substantially increase the fraction of destaining puncta nor the amount of destaining (**Supplementary Fig. 5a**,**b**) as would be expected if there were extensive leakage or spontaneous fusion. Moreover, non-destaining and destaining puncta exhibited similar mean fluorescence intensity immediately before stimulation (0.090 ± 0.005 a.u. versus 0.099 ± 0.005 a.u., respectively, for $n = 15$ slices from different mice, $P = 0.1840$ by unpaired two-tailed t test). Thus, although depletion of vesicular FFN200 may occur in some puncta, it is unlikely to be a major cause of the high fraction of unresponsive vesicle clusters.

As an alternative approach to estimate dopamine bouton activity, we used the endocytic dye FM1-43, which loads into recycling

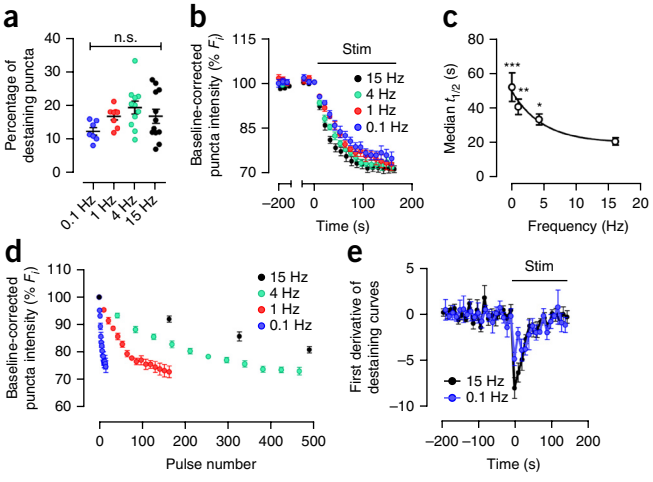

Figure 5 FFN200 release dependence on stimulus frequency in dorsal striatum. (**a**) Scatter plot of the percentage of destaining puncta in each independent experiment including mean ± s.e.m., for each indicated stimulation frequency ($n = 7$, 8, 11 and 12 for 0.1, 1, 4 and 15 Hz, respectively, for all panels of this figure, where n is number of mice with 1–2 slices averaged per mouse; n.s. indicates not significantly different, $P = 0.1039$ by one-way ANOVA). (**b**) Background-subtracted puncta fluorescence intensity over time, corrected for baseline fluorescence rundown (mean percentage of $F_i \pm$ s.e.m.). (**c**) Dependence of destaining $t_{1/2}$ with stimulation frequency (mean of the median $t_{1/2}$ for each independent experiment ± s.e.m.; $^{*}P < 0.05$, $^{**}P < 0.01$, $^{***}P < 0.001$, as determined by one-way ANOVA with Newman-Keuls multiple comparison test for the indicated frequencies when compared to 15 Hz). (**d**) Puncta destaining curves shown in **b** represented here as a function of stimulation pulse number. Error bars represent ± s.e.m. As images were acquired every 10–11 s, each acquisition point represents a different number of pulses at different frequencies (~1, 11, 42 and 162 pulses/acquisition point for 0.1, 1, 4 and 15 Hz, respectively; for comparison, only the first 500 pulses are represented). (**e**) First derivative of the puncta intensity versus time curves shown in **b** for 0.1 and 15 Hz. Error bars represent ±s.e.m. Error bars are included in all plots, but in some cases are occluded by the symbols.

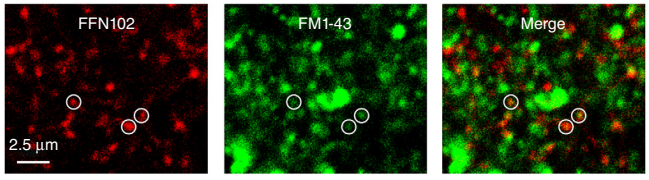

Figure 6 Identification of active presynaptic dopaminergic boutons in the dorsal striatum by FM1-43 loading. Representative images of striatal slices sequentially loaded with 10 µM FM1-43 (3,000 stimulation pulses at 15 Hz) and 15 µM FFN102 (10-min incubation). Specific activity-dependent FM1-43 puncta were identified as they disappeared following subsequent stimulation with 40 mM KCl. White circles indicate activity-dependent FM1-43 puncta that colocalized with FFN102.

synaptic vesicles as they undergo endocytosis[6]. In neuronal cultures, lack of FM1-43 loading has been used to identify 'presynaptically silent' synapses that were otherwise labeled with general synaptic markers[26–30]. FM1-43 was loaded into striatal presynaptic boutons by local stimulation at 15 Hz, and was followed by FFN102 loading to identify dopamine structures (FFN102 was used as it requires shorter washes than FFN200, rendering the long labeling protocol feasible). Given that FM1-43 shows substantial non-specific binding, we used subsequent KCl depolarization to identify the specific activity-dependent signal in recycling vesicles (data not shown).

We found that 10.4 ± 1.7% of activity-dependent FM1-43 puncta colocalized with FFN102 (n = 5 slices from different mice; **Fig. 6**). Notably, only 2.2 ± 0.5% of all FFN102 puncta loaded FM1-43 in an activity-dependent manner (**Fig. 6**). This corresponds to a density of 0.0026 ± 0.0006 puncta µm^{-3}, about 2.5% of the reported density of striatal dopaminergic synapses (see above). The difference in the fraction of responsive dopaminergic vesicle clusters assessed with FFN200 destaining and FM1-43 loading may be a result of FM1-43 nonspecific binding and low signal-to-noise ratio, or to an effect of the pre-stimulus required to load this probe on synaptic function. Nonetheless, both optical approaches suggest a large number of functionally silent dopamine vesicle clusters in response to electrical stimulation of the dorsolateral striatum.

FFN200 non-destaining puncta exhibit typical Ca^{2+} signals

To determine whether the high fraction of FFN200 non-destaining puncta was a consequence of inefficient stimulation or impaired Ca^{2+} influx, we investigated Ca^{2+} signaling at striatal dopamine axons. The genetically encoded Ca^{2+} indicator GCaMP3 was recently used in striatal dopamine axons to study the role of different Ca^{2+} channels in evoked Ca^{2+} transients, but individual bouton response was not assessed[31]. We generated transgenic mice expressing GCaMP3 in dopamine neurons by crossing the Ai38 floxed GCaMP3 reporter[32] and *DAT*^{IREScre} (ref. 33) mouse lines. We confirmed the specificity of GCaMP3 localization in midbrain VTA and SN dopamine neurons of resulting DAT-GCaMP3 mice by immunohistochemistry, using antibodies to GFP and TH to identify GCaMP3 and dopamine neurons, respectively (98.1 ± 0.1% of GCaMP3 cell bodies were labeled for TH, 100% of TH cell bodies were colabeled with GCaMP3; n = 2 mice, 2 fields of view per mouse, each with 20–39 cells; **Fig. 7a**,**b**). GCaMP3 was selectively expressed in dopamine axons, as the signal was mostly confined to the striatum and very low in the cortex and corpus callosum of striatal slices, matching the pattern of TH label (**Fig. 7c**). We found a high degree of colocalization between GCaMP3- and TH-positive axonal profiles (73.6 ± 3.4% of GCaMP3 structures expressed TH, 79.7 ± 7.4% of TH axonal profiles colabeled for GCaMP3; n = 2 mice, 2 fields of view per mouse, each with 198–350 axonal structures; **Fig. 7d**).

Imaging of GCaMP3 signals and FFN200 destaining from the same dopamine axonal structures was performed in striatal slices

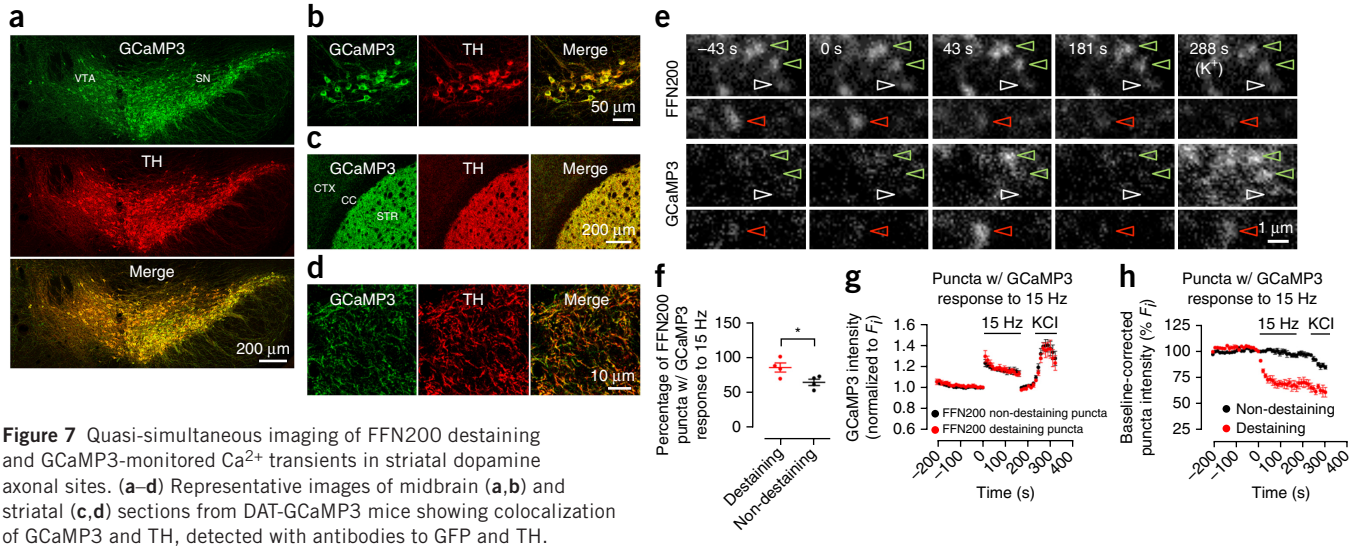

Figure 7 Quasi-simultaneous imaging of FFN200 destaining and GCaMP3-monitored Ca^{2+} transients in striatal dopamine axonal sites. (**a**–**d**) Representative images of midbrain (**a**,**b**) and striatal (**c**,**d**) sections from DAT-GCaMP3 mice showing colocalization of GCaMP3 and TH, detected with antibodies to GFP and TH. An overview of VTA and SN, obtained by a collage of three maximal projections acquired at low magnification, is shown in **a** and a higher magnification of SN is shown in **b**. Low- and high-magnification images are shown in **c** and **d**, respectively, of dorsal striatum GCaMP3 and TH signals (STR, striatum; CC, corpus callosum; CTX, cortex). (**e**) Representative images of FFN200 and GCaMP3 in the same fields of view in striatal slices (0 s, final time point before stimulation). Arrowheads indicate a destaining FFN200 punctum with increased GCaMP3 signal (red, bottom panels) and FFN200 non-destaining puncta with (green) or without (white) a GCaMP3 response to 15 Hz (top panels). (**f**) Scatter plot of the percentage of FFN200 destaining and non-destaining puncta with a GCaMP3 response to 15 Hz, including mean and s.e.m. (n = 4 slices from different mice for this and following panels; *P < 0.05, two-tailed unpaired t-test; P = 0.037). (**g**,**h**) Normalized amplitude of GCaMP3 fluorescence (**g**) and corresponding FFN200 intensity (**h**) in FFN200 destaining and non-destaining puncta showing a GCaMP3 response to 15 Hz (GCaMP3 signal: mean fold F_i ± s.e.m.; two-way ANOVA: P = 0.91 for destaining versus non-destaining comparison, P < 0.0001 for the effect of time, P = 1.0 for the interaction; FFN200 fluorescence: background and baseline-rundown corrected intensity as mean percentage of F_i ± s.e.m.).

by sequential line scanning of the two fluorophores. The fraction of FFN200-releasing puncta and $t_{1/2}$ of destaining in these experiments were 15.5 ± 1.1% and 16.8 ± 1.9 s (n = 4 slices from different mice), indicating that dopamine exocytosis was not affected in DAT-GCaMP3 animals. The vast majority of destaining puncta (85.2 ± 6.2%; **Fig. 7e**) showed substantial increases in GCaMP3 fluorescence intensity in response to 15-Hz stimulation (**Fig. 7f**). Notably, 65.0 ± 4.3% of non-destaining puncta also exhibited substantial increases in GCaMP3 signal following 15-Hz stimulation (**Fig. 7e**,**f**). Non-destaining puncta lacking a GCaMP3 response to 15 Hz (**Fig. 7e**) were either not efficiently stimulated by our procedure or exhibited Ca^{2+} signals below detection, as subsequent perfusion with 40 mM KCl induced GCaMP3 responses in 94.6 ± 2.6% (n = 4 slices from different mice) of these puncta.

The amplitudes of the 15-Hz evoked GCaMP3 signals in responsive puncta were not significantly different between FFN200 destaining and non-destaining cohorts (P = 0.91, two-way ANOVA; **Fig. 7g**). The amplitude of the GCaMP3 response to high K^+, although higher on average than that evoked by 15-Hz stimulation, was also similar between destaining and non-destaining puncta (**Fig. 7g**). Our results indicate that more than half of FFN200 non-destaining puncta exhibited Ca^{2+} signals that were indistinguishable from those detected in destaining puncta, suggesting that their lack of transmitter release is a result of a factor downstream from Ca^{2+} influx. We note, however, that Ca^{2+} microdomains in the puncta are not resolved by these techniques and that differences in small regions, including the vicinity of active zones, are expected to regulate synaptic vesicle fusion.

Puncta that displayed a GCaMP3 signal, but no FFN200 release, in response to 15-Hz stimulation showed a substantial decrease in FFN200 fluorescence when subsequently stimulated with high K^+ (**Fig. 7h**). In contrast, puncta that released FFN200 in response to 15-Hz stimuli displayed a significantly smaller response to KCl depolarization (KCl response slopes between time points 41 and 48: non-destaining puncta, −0.17 ± 0.04; destaining puncta, −0.07 ± 0.02; P = 0.049, two-tailed paired t test; **Fig. 7h**). Thus, under certain conditions, silent vesicle clusters can be recruited to release.

DISCUSSION

We developed FFN200 as the first fluorescent probe to label monoamine neurons in both primary neuronal cultures and brain slice, and used it to identify unexpected heterogeneity among striatal dopaminergic vesicle clusters. The activity-dependent destaining of this probe in the striatum was fully dependent on VMAT2, confirming FFN200 as a selective optical tracer of monoamine exocytosis. We found that only ~17% of striatal FFN200-labeled vesicle clusters released the probe following electrical stimulation. Independent assessment of synaptic exocytotic activity with the well-characterized probe FM1-43 was also consistent with a low density of active dopamine synapses. The majority of FFN200 non-destaining puncta, however, exhibited stimulation-dependent Ca^{2+} signals that were indistinguishable from those elicited at destaining puncta. These findings indicate that the majority of axonal sites containing synaptic vesicles capable of accumulating VMAT2 substrates are silent in response to activity-dependent Ca^{2+} influx in striatal slices.

FFN200 provides an effective tool for imaging exocytosis from striatal dopamine axons, as it is a monoamine-selective probe that does not require subsequent identification of monoamine boutons; its loading involves a simple incubation step and does not require transfection or any pre-stimulation steps that may cause synaptic plasticity, in contrast with synaptopHluorins and FM1-43; it is the first developed FFN that labels dopamine vesicle clusters both in neuronal cultures and in brain slices; and its pH-independent fluorescence enables a more accurate monitoring of destaining kinetics than the pH-dependent FFN102.

Although FFN102 loading is strictly DAT dependent[13], FFN200 does not rely on DAT to enter the cell, and the means by which it crosses the plasma membrane are currently unknown. FFN200 specificity toward dopamine neuron cell bodies in culture is high, suggesting that the diffuse FFN200 signal throughout the cell relies on either an active Na^+-independent cell-specific mechanism of loading or the presence of a cytosolic factor that retains FFN200 specifically in dopaminergic cells. FFN200 accumulation in striatal axonal sites was partly VMAT2 dependent: puncta intensity was reduced by ~30% and the entire distribution of intensities of individual puncta was shifted to lower values when VMAT2 function or expression was inhibited (**Fig. 2d**–**f**), suggesting that the majority of puncta accumulate FFN200 in VMAT2-containing compartments. Notably, no activity-induced release of FFN200 was observed in VMAT2 hypomorph striatum (**Fig. 3a**,**b**). Together, these results suggest that ~30% of the total FFN200 signal is in VMAT2-expressing compartments and can be destained in response to stimulation, providing a straightforward means to measure exocytosis from striatal dopaminergic axonal boutons, the primary monoaminergic input to the striatum[16,17].

The kinetics of FFN200 destaining from striatal boutons at high stimulation frequency is comparable to the kinetics of FM dye release in midbrain dopamine neuronal cultures[9] and hippocampal slice CA3-CA1 synapses[34] ($t_{1/2s}$ of ~25 s at 10 Hz). At lower stimulation frequencies, however, FFN200 release from striatal boutons was faster than FM1-43 release from glutamatergic synapses ($t_{1/2}$ of ~130 s at 1 Hz)[34]. This parallels the high level of dopamine release recorded electrochemically in the slice preparation in response to a single stimulus (or the first of a train of pulses)[22,23], which is mostly attributed to nicotinic receptor activation[35,36]. Dopamine release decreases sharply in response to subsequent stimuli in a frequency-dependent manner (higher frequencies result in higher inhibition)[22,23,35,36]. Our results are therefore consistent with the kinetics of dopamine release measured by CV and they further suggest that the high level of single pulse–evoked dopamine release is a result of exocytosis of a considerable fraction of releasable vesicles (~17%; **Fig. 5d**,**e**). In comparison, glutamate synapses release less than 1% of their vesicle pool per action potential measured, however, by a technique with a different readout mechanism (endocytic dyes)[34].

FFN200 imaging at striatal dopamine axons revealed a surprisingly small fraction of destaining vesicle clusters in response to stimulation. It seems unlikely that the large cohort of unresponsive puncta represent axonal areas lacking labeled synaptic vesicles given that the density of FFN200 puncta was similar to the reported density of dopamine synapses in rat striatum[24,25], the majority of FFN200 puncta showed decreased fluorescence intensity following VMAT2 knockdown or inhibition, and the fraction of FFN102-tagged striatal dopamine axonal sites that loaded the endocytic probe FM1-43 was very low (**Fig. 5**). Moreover, the majority of non-destaining puncta displayed electrically evoked Ca^{2+} signals that were indistinguishable from those in destaining puncta, as monitored by GCaMP3 imaging (**Fig. 6f**,**g**). FFN200 non-releasing axonal sites therefore contain the probe in VMAT2-expressing vesicles and exhibit Ca^{2+} influx in response to stimulus trains, but fail to release transmitter.

Although release in response to a single stimulus can be measured with this approach, we cannot exclude the possibility that non-destaining puncta release a low amount of FFN200 that is below detection limits. Techniques resolving single-vesicle exocytosis in the brain slice will be required to address this issue. Our results also do not address

whether a similarly high fraction of non-releasing vesicle clusters occurs *in vivo* or how the slice preparation may affect factors that regulate neurotransmission. We note, however, that FFN200 release was observed in response to KCl stimulation from puncta that did not destain in response to 15 Hz, suggesting that some silent vesicle clusters are capable of release under certain conditions.

Presynaptically silent synapses were initially proposed in studies of the neuromuscular junction and motoneuron synapses[37–39] and have been recently described in hippocampal glutamatergic[26–28] and GABAergic[29,40] neurons, and cerebellar granule neurons[30,41]. Our study represents, to the best of our knowledge, a first report on silent neuromodulatory synapses. Moreover, the ability of FFN200 to label both active and silent vesicle clusters enabled, to the best of our knowledge, the first direct quantification of presynaptically silent synapses in brain tissue. The absence of exocytosis in silent dopaminergic vesicle clusters could be a result of multiple mechanisms, including a local inhibitory factor impairing vesicle fusion downstream from Ca^{2+} entry or the lack of a component essential for exocytosis. Previous reports have suggested that modulation of vesicle priming, for example, may underlie presynaptic silencing[42,43]. Another possibility would be lack of an active zone in close proximity to most FFN-labeled vesicle clusters; note, however, that the density of striatal dopamine synapses, as defined by a cluster of vesicles juxtaposed to symmetric membrane densities, closely matches the density of FFN200 puncta. It is unlikely that the majority of non-destaining vesicle clusters represent synaptic vesicles traveling along the axon en route to an actual synapse, as the majority of puncta (>95%) remained stationary for imaging periods up to ~13 min (data not shown).

Given that dopaminergic axons cover very extensive areas in the striatum[44], restricting dopamine release to a minority of axonal sites would confer spatial selectivity to the modulation of striatal synapses by dopamine. Small 'hot spots' of high dopamine release have been reported in response to sucrose and ethanol-directed behaviors[45,46]. Silent axonal sites could underlie the size and location of such hot spots. Silent dopamine vesicle clusters may also be involved in the formation of new release sites, as suggested for presynaptically silent glutamatergic synapses in the hippocampus[47–49]. Indeed, a theory of motor learning in the cerebellum assumes a preponderance of presynaptically silent granule cell synapses[50] and may be a useful model for basal ganglia learning. Finally, the state of silent vesicle clusters may be important in disorders such as schizophrenia, which show striatal hyperdopaminergia and cortical hypodopaminergia, and processes of 'unsilencing' may have clinical applications for diseases such as Parkinson's disease.

METHODS

Methods and any associated references are available in the online version of the paper.

Note: Any Supplementary Information and Source Data files are available in the online version of the paper.

ACKNOWLEDGMENTS

We thank M. Caron (Duke University) for providing DAT knockout mice, A. Salahpour (University of Toronto) and G. Miller (Emory University) for the VMAT2 hypomorph, mice and K. Kobayashi (Fukushima Medical University) for the TH-GFP mice. We would also like to thank C. Castagna, V. Morales, A. Barnett and D. Korostyshevsky for excellent technical support as well as other members of the Sulzer and Sames laboratories for helpful discussions and support. This work was supported by the G. Harold & Leila Y. Mathers Charitable Foundation (D. Sames), National Institute on Mental Health (R01MH086545 to D. Sames, R01MH108186 to D. Sames and D. Sulzer), the J.P.B. (D. Sulzer), McKnight (D. Sames and D. Sulzer) and Parkinson's Disease Foundations (D. Sulzer), the National Institute on Drug Abuse (DA07418 and DA10154; D. Sulzer), the National Institute on Alcohol Abuse and Alcoholism (AA019801; D. Sulzer), and a National Institute of Neurological Disorders and Stroke (NINDS) Udall Center of Excellence for Parkinson's Disease Research (D. Sulzer). Y.S. was supported by the Michael J. Fox Foundation, J.E.L.-O. was supported by NINDS (3 P50 NS 038370-13S1), P.C.R. was granted a pre-doctoral fellowship by the National Science Foundation and E.V.M. was funded by NINDS (R01NS075222).

AUTHOR CONTRIBUTIONS

D.B.P., Y.S., E.V.M., D. Sulzer and D. Sames conceived and designed the experiments. S.L. conducted the early examination of FFN200 in brain tissue. D.B.P., P.M. and P.C.R. performed slice imaging probe characterization experiments and Y.S. and E.V.M. performed cell culture imaging experiments. D.B.P. performed brain slice FFN200 destaining experiments, including FFN200-GCaMP3 simultaneous imaging. J.M., aided by D.B.P., developed the Matlab image analysis routine and T.J.M. contributed with additional data output scripts. D. Sames designed FFN200, and G.H. and A.H. designed and performed FFN200 synthesis and purification as well as chemical and photophysical characterization. R.J.K. performed the FFN200 K_m determination experiments. J.E.L.-O. designed and performed the CV experiments. M.S.S. aided with the FFN200-GCaMP3 simultaneous imaging experiments. E.K. optimized and provided midbrain dopamine cultures. D.B.P., Y.S., P.M., J.E.L.-O., R.J.K., P.C.R. and E.V.M. analyzed data. D.B.P. wrote the paper, with important contributions from Y.S., J.M., M.S.S., E.V.M., P.C.R., D. Sulzer and D. Sames.

COMPETING FINANCIAL INTERESTS

The authors declare competing financial interests: details are available in the online version of the paper.

1. Zhang, M.Y. & Beyer, C.E. Measurement of neurotransmitters from extracellular fluid in brain by in vivo microdialysis and chromatography-mass spectrometry. *J. Pharm. Biomed. Anal.* **40**, 492–499 (2006).
2. Schmitz, Y., Lee, C.J., Schmauss, C., Gonon, F. & Sulzer, D. Amphetamine distorts stimulation-dependent dopamine overflow: effects on D2 autoreceptors, transporters, and synaptic vesicle stores. *J. Neurosci.* **21**, 5916–5924 (2001).
3. Kennedy, R.T., Jones, S.R. & Wightman, R.M. Simultaneous measurement of oxygen and dopamine: coupling of oxygen consumption and neurotransmission. *Neuroscience* **47**, 603–612 (1992).
4. Bérubé-Carrière, N. *et al.* Ultrastructural characterization of the mesostriatal dopamine innervation in mice, including two mouse lines of conditional VGLUT2 knockout in dopamine neurons. *Eur. J. Neurosci.* **35**, 527–538 (2012).
5. Pickel, V.M., Beckley, S.C., Joh, T.H. & Reis, D.J. Ultrastructural immunocytochemical localization of tyrosine hydroxylase in the neostriatum. *Brain Res.* **225**, 373–385 (1981).
6. Betz, W.J. & Bewick, G.S. Optical analysis of synaptic vesicle recycling at the frog neuromuscular junction. *Science* **255**, 200–203 (1992).
7. Miesenböck, G., De Angelis, D.A. & Rothman, J.E. Visualizing secretion and synaptic transmission with pH-sensitive green fluorescent proteins. *Nature* **394**, 192–195 (1998).
8. Onoa, B., Li, H., Gagnon-Bartsch, J.A., Elias, L.A. & Edwards, R.H. Vesicular monoamine and glutamate transporters select distinct synaptic vesicle recycling pathways. *J. Neurosci.* **30**, 7917–7927 (2010).
9. Mani, M. & Ryan, T.A. Live imaging of synaptic vesicle release and retrieval in dopaminergic neurons. *Front. Neural Circuits* **3**, 3 (2009).
10. Pan, P.Y. & Ryan, T.A. Calbindin controls release probability in ventral tegmental area dopamine neurons. *Nat. Neurosci.* **15**, 813–815 (2012).
11. Daniel, J.A., Galbraith, S., Iacovitti, L., Abdipranoto, A. & Vissel, B. Functional heterogeneity at dopamine release sites. *J. Neurosci.* **29**, 14670–14680 (2009).
12. Gubernator, N.G. *et al.* Fluorescent false neurotransmitters visualize dopamine release from individual presynaptic terminals. *Science* **324**, 1441–1444 (2009).
13. Rodriguez, P.C. *et al.* Fluorescent dopamine tracer resolves individual dopaminergic synapses and their activity in the brain. *Proc. Natl. Acad. Sci. USA* **110**, 870–875 (2013).
14. Liu, Y. *et al.* A cDNA that suppresses MPP+ toxicity encodes a vesicular amine transporter. *Cell* **70**, 539–551 (1992).
15. Matsushita, N. *et al.* Dynamics of tyrosine hydroxylase promoter activity during midbrain dopaminergic neuron development. *J. Neurochem.* **82**, 295–304 (2002).
16. Fuxe, K., Hökfelt, T., Olson, L. & Ungerstedt, U. Central monoaminergic pathways with emphasis on their relation to the so called 'extrapyramidal motor system'. *Pharmacol. Ther. [B]* **3**, 169–210 (1977).
17. Pickel, V.M., Nirenberg, M.J. & Milner, T.A. Ultrastructural view of central catecholaminergic transmission: immunocytochemical localization of synthesizing enzymes, transporters and receptors. *J. Neurocytol.* **25**, 843–856 (1996).
18. Thompson, L., Barraud, P., Andersson, E., Kirik, D. & Björklund, A. Identification of dopaminergic neurons of nigral and ventral tegmental area subtypes in grafts of fetal ventral mesencephalon based on cell morphology, protein expression, and efferent projections. *J. Neurosci.* **25**, 6467–6477 (2005).

19. Caudle, W.M. *et al.* Reduced vesicular storage of dopamine causes progressive nigrostriatal neurodegeneration. *J. Neurosci.* **27**, 8138–8148 (2007).
20. Mooslehner, K.A. *et al.* Mice with very low expression of the vesicular monoamine transporter 2 gene survive into adulthood: potential mouse model for parkinsonism. *Mol. Cell. Biol.* **21**, 5321–5331 (2001).
21. Grace, A.A. & Bunney, B.S. The control of firing pattern in nigral dopamine neurons: burst firing. *J. Neurosci.* **4**, 2877–2890 (1984).
22. Kennedy, R.T., Jones, S.R. & Wightman, R.M. Dynamic observation of dopamine autoreceptor effects in rat striatal slices. *J. Neurochem.* **59**, 449–455 (1992).
23. Abeliovich, A. *et al.* Mice lacking alpha-synuclein display functional deficits in the nigrostriatal dopamine system. *Neuron* **25**, 239–252 (2000).
24. Arbuthnott, G.W. & Wickens, J. Space, time and dopamine. *Trends Neurosci.* **30**, 62–69 (2007).
25. Groves, P.M., Linder, J.C. & Young, S.J. 5-hydroxydopamine-labeled dopaminergic axons: three-dimensional reconstructions of axons, synapses and postsynaptic targets in rat neostriatum. *Neuroscience* **58**, 593–604 (1994).
26. Altrock, W.D. *et al.* Functional inactivation of a fraction of excitatory synapses in mice deficient for the active zone protein bassoon. *Neuron* **37**, 787–800 (2003).
27. Rosenmund, C. *et al.* Differential control of vesicle priming and short-term plasticity by Munc13 isoforms. *Neuron* **33**, 411–424 (2002).
28. Moulder, K.L. *et al.* Plastic elimination of functional glutamate release sites by depolarization. *Neuron* **42**, 423–435 (2004).
29. Kannenberg, K., Sieghart, W. & Reuter, H. Clusters of GABAA receptors on cultured hippocampal cells correlate only partially with functional synapses. *Eur. J. Neurosci.* **11**, 1256–1264 (1999).
30. Cousin, M.A. & Evans, G.J. Activation of silent and weak synapses by cAMP-dependent protein kinase in cultured cerebellar granule neurons. *J. Physiol. (Lond.)* **589**, 1943–1955 (2011).
31. Sgobio, C. *et al.* Optogenetic measurement of presynaptic calcium transients using conditional genetically encoded calcium indicator expression in dopaminergic neurons. *PLoS One* **9**, e111749 (2014).
32. Zariwala, H.A. *et al.* A Cre-dependent GCaMP3 reporter mouse for neuronal imaging *in vivo*. *J. Neurosci.* **32**, 3131–3141 (2012).
33. Bäckman, C.M. *et al.* Characterization of a mouse strain expressing Cre recombinase from the 3′ untranslated region of the dopamine transporter locus. *Genesis* **44**, 383–390 (2006).
34. Zakharenko, S.S., Zablow, L. & Siegelbaum, S.A. Visualization of changes in presynaptic function during long-term synaptic plasticity. *Nat. Neurosci.* **4**, 711–717 (2001).
35. Zhang, H. & Sulzer, D. Frequency-dependent modulation of dopamine release by nicotine. *Nat. Neurosci.* **7**, 581–582 (2004).
36. Rice, M.E. & Cragg, S.J. Nicotine amplifies reward-related dopamine signals in striatum. *Nat. Neurosci.* **7**, 583–584 (2004).
37. Jahromi, S.S. & Atwood, H.L. Three-dimensional ultrastructure of the crayfish neuromuscular apparatus. *J. Cell Biol.* **63**, 599–613 (1974).
38. Hirst, G.D., Redman, S.J. & Wong, K. Post-tetanic potentiation and facilitation of synaptic potentials evoked in cat spinal motoneurones. *J. Physiol. (Lond.)* **321**, 97–109 (1981).
39. Bennett, M., Jones, P. & Lavidis, N. Transmitter secretion varies between visualized release sites at amphibian neuromuscular junctions. *Neurosci. Lett.* **65**, 311–315 (1986).
40. Losonczy, A., Biró, A.A. & Nusser, Z. Persistently active cannabinoid receptors mute a subpopulation of hippocampal interneurons. *Proc. Natl. Acad. Sci. USA* **101**, 1362–1367 (2004).
41. Chavis, P., Mollard, P., Bockaert, J. & Manzoni, O. Visualization of cyclic AMP-regulated presynaptic activity at cerebellar granule cells. *Neuron* **20**, 773–781 (1998).
42. Moulder, K.L., Jiang, X., Taylor, A.A., Olney, J.W. & Mennerick, S. Physiological activity depresses synaptic function through an effect on vesicle priming. *J. Neurosci.* **26**, 6618–6626 (2006).
43. Jiang, X. *et al.* A role for the ubiquitin-proteasome system in activity-dependent presynaptic silencing. *J. Neurosci.* **30**, 1798–1809 (2010).
44. Matsuda, W. *et al.* Single nigrostriatal dopaminergic neurons form widely spread and highly dense axonal arborizations in the neostriatum. *J. Neurosci.* **29**, 444–453 (2009).
45. Cacciapaglia, F., Wightman, R.M. & Carelli, R.M. Rapid dopamine signaling differentially modulates distinct microcircuits within the nucleus accumbens during sucrose-directed behavior. *J. Neurosci.* **31**, 13860–13869 (2011).
46. Robinson, D.L., Howard, E.C., McConnell, S., Gonzales, R.A. & Wightman, R.M. Disparity between tonic and phasic ethanol-induced dopamine increases in the nucleus accumbens of rats. *Alcohol. Clin. Exp. Res.* **33**, 1187–1196 (2009).
47. Choi, S., Klingauf, J. & Tsien, R.W. Postfusional regulation of cleft glutamate concentration during LTP at 'silent synapses'. *Nat. Neurosci.* **3**, 330–336 (2000).
48. Ma, L., Zablow, L., Kandel, E.R. & Siegelbaum, S.A. Cyclic AMP induces functional presynaptic boutons in hippocampal CA3-CA1 neuronal cultures. *Nat. Neurosci.* **2**, 24–30 (1999).
49. Voronin, L.L. *et al.* Postsynaptic depolarisation enhances transmitter release and causes the appearance of responses at "silent" synapses in rat hippocampus. *Neuroscience* **126**, 45–59 (2004).
50. Porrill, J. & Dean, P. Silent synapses, LTP, and the indirect parallel-fibre pathway: computational consequences of optimal cerebellar noise-processing. *PLoS Comput. Biol.* **4**, e1000085 (2008).

ONLINE METHODS

Materials. FFN200 and FFN102 were synthetized in our laboratories. (+)−(2R,3R,11bR)-alpha-dihydrotetrabenazine (dTBZ) was a gift from the National Institute of Mental Health (NIMH) Chemical Synthesis and Drug supply program (http://nimh-repository.rti.org/) while racemic TBZ, used for K_m determination, was from Sigma-Aldrich. The anti-TH mouse monoclonal (MAB5280) and rabbit polyclonal (657012) antibodies as well as the anti-GFP rabbit polyclonal antibody (AB3080) were from Millipore/Calbiochem, the mouse monoclonal anti-synaptophysin antibody (IR776; clone SY38) was from DAKO and the mouse monoclonal anti-calbindin D-28K antibody (C9848; clone CB-955) was from Sigma-Aldrich. Secondary anti-mouse and anti-rabbit antibodies conjugated to either Alexa 488 or Alexa 594, as well as FM1-43, were from Molecular Probes (Life Technologies) and the ADVASEP-7 was from Cydex Pharmaceuticals. HEPES, DMEM and FBS were from Invitrogen (Life Technologies). AP-5, NBQX and TTX were from Tocris Bioscience. All other reagents were from Sigma-Aldrich.

FFN200 nuclear magnetic resonance (NMR) characterization and molecular weight determination. FFN200 was prepared as a FFN200 HCl salt of pale yellow appearance. ^{1}H NMR and ^{13}C NMR spectra were recorded on Bruker 400 MHz NMR spectrometer. Proton chemical shifts δ are expressed in parts per million (p.p.m.) and are referenced to residual proton in the NMR solvent (D_2O, δ = 4.79 p.p.m.). Data for ^{1}H NMR are reported as follows: chemical shift, multiplicity (s = singlet, d = doublet, *t* = triplet, m = multiplet, br. = broad peak), coupling constant in Hz, integration. Carbon chemical shifts are referenced to the carbon resonance of the NMR solvent (CD_3OD, δ = 49.0 p.p.m.). Mass spectra were recorded on a JEOL LCmate instrument (ionization mode: APCI$^+$). ^{1}H NMR (400 MHz, D_2O): δ 7.68 (d, *J* = 8.7 Hz, 1H, *H*-5), 7.04 (dd, *J* = 8.7, 2.2 Hz, 1H, *H*-6), 6.97 (d, *J* = 2.2 Hz, 1H, *H*-8), 6.26 (s, 1H, *H*-3), 3.39 (t, *J* = 7.5 Hz, 2H, N-CH_2), 3.21 (t, *J* = 7.5 Hz, 2H, CH_2). ^{13}C NMR (101 MHz, CD_3OD): δ 164.0, 157.7, 155.1, 154.0, 126.5, 113.3, 109.5, 109.2, 100.8, 39.5, 30.4. LRMS (APCI$^+$): Calculated for $C_{11}H_{12}N_2O_2$ 204.1, measured 205.2 (***M***H$^+$). The molecular weight of FFN200 HCl salt was determined by ^{1}H NMR spectroscopy in CD_3OD with 1,4-dimethoxybenzene as an internal standard. Found molecular weight of 275.6 g mol^{-1} corresponds to FFN200 with two molecules of HCl.

FFN200 photophysical characterization. Fluorescence excitation and emission spectra of FFN200 were acquired on a Jobin Yvon Fluorolog fluorescence spectrofluorometer (Horiba). Fluorescence measurements were taken of a final probe concentration of 5 μM in potassium phosphate buffer with pH adjusted to 7.4.

FFN200 logD measurement. LogD was determined according to the European Union Organization for Economic Cooperation and Development Guideline for the Testing of Chemicals (Section 1: Physical Chemical Properties, Test No. 107). A traditional shake flask method was employed in the test. The probe concentration in octanol and aqueous layers was determined using fluorimetry and subsequently fitting the respective values onto calibration curves. All measurements were performed at three different concentrations in duplicate. Probe stock solution was added to a mixture of octanol and pH 7.4 potassium phosphate buffer and thoroughly mixed by inverting the tube at least 100 times and subsequently spinning at 3,000 rpm for 5 min to facilitate phase separation. The probe concentrations in each layer were determined by interpolation from standard curves of fluorescence emission of the probe against concentration. LogD was calculated based on the equation: $\log D = \log[\text{probe}]_{\text{octanol}} - \log[\text{probe}]_{\text{buffer}}$, where $[\text{probe}]_{\text{octanol}}$ and $[\text{probe}]_{\text{buffer}}$ are measured concentrations of the probe in n-octanol and pH 7.4 potassium phosphate buffer, respectively.

Determination of FFN200 K_m. The human embryonic kidney cells stably transfected with VMAT2, described previously[51], were used. Functional VMAT2 expression in these cells was previously validated by western blot, immunocytochemistry, [^{3}H]dTBZ binding and [^{3}H]serotonin uptake[51]. Cells were plated at 0.03–0.04 × 10^6 cells per well in poly-D-lysine–coated (0.1 mg ml^{-1}) 96-well plates. No signs of mycoplasma contamination were observed by nuclear staining. After reaching confluence (~3 d), cells were incubated with TBZ (2 μM, 100 μl per well) or DMSO vehicle (0.02%) for 1 h in experimental medium (DMEM without phenol red containing 25 mM HEPES and 1% FBS). Cells were then incubated with FFN200 at different concentrations (50, 25, 12.5, 6, 3, and 1 μM), together with 2 μM TBZ or DMSO in experimental medium, for 12 min at 22–24 °C. FFN200 uptake was terminated by washing with PBS and fluorescence was measured in each well with a BioTek H1MF plate reader (BioTek) in bottom read mode with excitation and emission wavelengths of 352 nm and 451 nm, respectively. The specific uptake at each concentration of FFN200 was determined by subtracting the fluorescence intensity of TBZ-treated cells from that of uninhibited (DMSO-treated) cells, and was linear for concentrations of FFN200 of 50 μM or less for times up to 12 min. The initial rates of specific uptake for each concentration were fit to the Michaelis-Menten equation using GraphPad Prism 5 (GraphPad Software) to derive the K_m value for FFN200 uptake by VMAT2. Each experiment consisted of duplicate plates, and K_m was calculated from the mean of three independent experiments.

Mice. All animal protocols followed US National Institutes of Health guidelines and were approved by Columbia University's Institutional Animal Care and Use Committee. Mice were housed in groups of five or less per cage, in a 12-h day/12-h night cycle with ad libitum access to food and water. TH-GFP mice[15] were kindly provided by K. Kobayashi (Fukushima Medical University) and the DAT KO mice[52] were a kind gift of M. Caron (Duke University). A. Salahpour (University of Toronto) kindly provided the VMAT2 hypomorph mice[19,20]. Wild-type C57BL/6 mice and the *DAT*^{IREScre} (ref. 33, strain name: B6.SJL-*Slc6a3*$^{tm1.1(cre)Bkmn}$/J) and Ai38 floxed GCaMP3 reporter[32] (strain name: B6;129S-*Gt(ROSA)26Sor*$^{tm38(CAG-GCaMP3)Hze}$/J) mouse lines were obtained from The Jackson Laboratory. To obtain transgenic mice expressing GCaMP3 in dopamine neurons, we crossed the Ai38 floxed GCaMP3 reporter and *DAT*^{IREScre} mouse lines. The Ai38 mice express GCaMP3 from the *ROSA26* locus, driven by a *CAG* promoter, in a Cre-dependent manner due to the presence of a *lox-stop-lox* cassette. Crossing with *DAT*^{IREScre} mice, which express the Cre recombinase under the transcriptional control of the endogenous DAT promoter, leads to selective GCaMP3 expression in DAT-expressing tissues. *DAT*$^{IREScre/wt}$ heterozygous mice were crossed with heterozygous Ai38 mice and the resulting heterozygous mice for both transgenes were identified by PCR according to protocols provided on the vendor's website and used in all GCaMP3 imaging experiments. We termed these animals "DAT-GCaMP3" mice.

Preparation of wild-type and transgenic mouse brain slices. Striatal slices were prepared as previously described[13], with minor modifications. Briefly, 7–12 week-old mice were killed by cervical dislocation and decapitated. Wild-type male mice were used and in the case of the transgenic mice, both female and male DAT-GCaMP3 animals were used (due to limited number of animals available), while sex-matched transgene and control littermates were used in experiments with DAT knockouts and VMAT2 hypomorphs. Three of five sets of VMAT2 hypomorph and wild-type littermates were 16–22 weeks old. Since results did not differ between animals of different age, data from both groups were pooled together. Acute 250 μm thick coronal brain slices were cut on a Leica VT1200 vibratome (Leica Microsystems), kept at 22–25 °C in oxygenated (95% O_2, 5% CO_2) artificial cerebrospinal fluid (ACSF [in mM]: 125.2 NaCl, 2.5 KCl, 26 $NaHCO_3$, 0.3 KH_2PO_4, 2.4 $CaCl_2$, 1.3 $MgSO_4$, 10 glucose, 0.8 HEPES, pH 7.3–7.4, 295–305 mOsm), and used within 1–5 h.

Cell culture preparation. Ventral midbrain neuronal cultures derived from postnatal day 0–3 mouse pups were prepared as previously described[53]. A detailed protocol is available on our laboratory's website (http://sulzerlab.org/Sulzer_VM_culture_protocol_book_version6%201.pdf). Briefly, neurons were dissociated and plated at a density of approximately 100,000 neurons cm^{-2} on a layer of rat cortical glial cells grown on either round glass coverslips or glass bottom culture dishes. They were maintained in culture medium supplemented with 10 ng ml^{-1} glial cell line–derived neurotrophic factor in a 5% CO_2 incubator at 37 °C for 2–3 weeks.

FFN loading and imaging. *Brain slices.* Striatal slices were incubated in ACSF with 10 μM FFN for 30 min at 22–24 °C and washed for 20 min in the case of FFN102 or 45–50 min for FFN200 (a washout of at least 45 min is needed to ensure optimal selectivity toward striatal dopamine boutons; not shown), unless otherwise indicated. For the DAT and VMAT2 inhibition experiments, slices were pre-incubated with either 5 μM nomifensine for 15 min or 5 μM dTBZ for 1 h before FFN200 incubation in the presence of 5 μM of the corresponding inhibitor.

doi:10.1038/nn.4252

Slices were then washed for 45 min in the absence of any drugs before the onset of imaging. For the DAT KO and VMAT2 hypomorph experiments, wild-type and transgenic slices were imaged on the same day, at approximately the same time after sectioning, under the same conditions. For TH-GFP colocalization and pharmacology experiments, slices were imaged by two-photon microscopy on a Leica SP5 confocal/multi-photon microscope (Leica Microsystems) equipped with a Spectra-Physics BB titanium-sapphire pulsed laser (Newport) and either a 40× 0.8 NA (Olympus; TH-GFP colocalization experiments) or a 63× 0.9 NA (Leica Microsystems; dTBZ and nomifensine inhibition experiments) water immersion objective. For all other experiments, slices were imaged on Prairie Ultima Multiphoton Microscopy Systems (Bruker/Prairie Technologies) equipped either with a Spectra-Physics MaiTai HP DeepSee titanium-sapphire pulsed laser (Newport) or Coherent Chameleon Ultra II and Vision II titanium-sapphire pulsed lasers (Coherent) and either a 60× 0.9 NA (Olympus) or a 63× 1.0 NA (Carl Zeiss Microscopy) water immersion objective. Slices were placed in a QE-1 imaging chamber (Warner Instruments), held in place with a custom-made platinum wire and nylon holder[54], and superfused with oxygenated ACSF (2–3 ml min^{-1}) using an Instech peristaltic pump (Instech Laboratories). All images were acquired at a depth of at least 30 µm. TH-GFP colocalization experiments were performed on the Leica microscope as described previously[13]. Briefly, FFN200 and GFP were detected by sequential imaging of the same sample field (single z-plane 8-bit images; 38 × 38 µm field of view; 512 × 512 pixel resolution) using the following parameters: GFP was excited at 910–920 nm and detected in the wavelength range of 510–600 nm; FFN200 was excited at 760 nm and detected at 440–490 nm. Lack of signal bleed-through between the FFN200 and GFP channels was confirmed by acquiring FFN200-GFP image sequences in FFN200-incubated wild type slices and in TH-GFP slices devoid of FFN200. To avoid underestimating GFP-FFN200 colocalization due to shifts in the z-plane, we acquired FFN200-GFP-FFN200 sequences and discarded any sequences showing less than 85% colocalization between the first and second FFN images. All other FFN200 imaging experiments were performed using excitation wavelengths of 740–770 nm and an emission range of 440–500 nm. For nomifensine and dTBZ experiments, single z-plane 8-bit images were acquired on the Leica two-photon microscope with a size of 41 × 41 µm at 512 × 512 pixel resolution. For the DAT KO and VMAT2 hypomorph experiments, single z-plane 12-bit images were acquired on a Prairie two-photon microscope with a 38 × 38 µm field of view at 512 × 512 pixel resolution. Imaging parameters for the KCl and electrical destaining experiments, including the ones using DAT-GCaMP3 mice, will be detailed in a following section. All live brain slice imaging experiments were conducted at 22–24 °C.

Cell culture. Ventral midbrain neuronal cultures prepared as above on glass coverslips were incubated for 30 min at 37 °C with 10 or 20 µM FFN200 in the presence of 50 µM AP-5 and 10 µM NBQX, in culture medium. Cultures were then transferred into closed imaging chambers (RC-21BRFS, 260 µl volume, Warner Instruments) and perfused (0.5 ml min^{-1}) with Tyrode's solution (in mM: 119 NaCl, 2.5 KCl, 25 HEPES sodium salt, 2 $MgCl_2$, 2 $CaCl_2$, 30 glucose, 50 µM AP-5, 10 µM NBQX, pH 7.5; osmolarity, 320 mOsm) at 24–26 °C. Following at least 10 min of Tyrode's superfusion to wash out FFN200, images were acquired using MetaMorph software (Molecular Devices) on an Olympus IX8-ZDC inverted fluorescence microscope with focus drift compensation (Olympus) equipped with a ProScan digitized stage (Prior Scientific) and a Photometrics Cool Snap HQ camera (Roper Scientific). For high potassium destaining experiments, images were acquired every 5 s at 200 ms exposure time using a 60× 1.35 NA oil objective (Olympus), a fluorescence filter set for DAPI (#3100v2; Chroma Technology) and a 1.3 neutral density filter. Solutions were switched from regular Tyrode's to 90 mM KCl-containing Tyrode's solution (in mM: 31.5 NaCl, 90 KCl, other components same), for at least 1 min, with a perfusion valve control system (Warner Instruments). For immunostaining experiments, stage positions of FFN200-labeled cell bodies were recorded before fixation. For synaptophysin staining, fixative was added to the culture dish while FFN200 images were being acquired. This method allowed us to minimize underestimating the colocalization between FFN200 and synaptophysin caused by movement of FFN-labeled organelles. FFN200, calbindin and TH colocalization images were acquired on a Zeiss Axiovert 100 microscope equipped with a Zeiss AxioCam MRm camera using a 20 × 0.5 NA objective (Carl Zeiss Microscopy).

Immunocytochemisty. Cultures were fixed with 4% paraformaldehyde for 5 min at 22–24 °C, followed by 10 min in 100% methanol at −20 °C. Cultures were then stained overnight at 4 °C with anti-calbindin antibody at 1:400, anti-TH antibody at 1:500–1:1,000 or anti-synaptophysin antibody at 1:100, followed by incubation with secondary antibodies conjugated to Alexa Fluor 350, 488 or 594, at 1:200, for 1 h at 22–24 °C.

Immunohistochemistry and imaging of DAT-GCaMP3 mouse brain cryosections. DAT-GCaMP3 mice were superfused with phosphate-buffered 4% paraformaldehyde and their brains were postfixed overnight and cryoprotected in 30% sucrose for 2 d. Coronal cryosections of the midbrain and striatum were cut at 30–40-µm thickness and blocked overnight in phosphate buffered saline with 0.03% Triton (PBS-T) and 10% normal donkey serum (NDS). Sections were immunostained with rabbit anti-GFP (1:500) and mouse anti-TH (1:1,000) antibodies overnight at 4 °C (in PBS-T with 2% NDS), following by a 1 h incubation at 22–24 °C in donkey anti-rabbit Alexa 488 and anti-mouse Alexa 594 antibodies (both 1:400). The two fluorophores were visualized on mounted sections by sequential imaging using the Leica SP5 confocal/multi-photon microscope (Leica Microsystems) using the Argon 488 and DPSS 561 lasers and emission wavelengths of 500–550 and 590–680 nm, respectively. No signal bleed-through was observed between channels when imaging single-stained slices, using these conditions. Low magnification images of the ventral midbrain and dorsolateral striatum were taken with a 10× 0.3 NA dry objective (stacks of *z* sections taken every 5 µm in a volume of 25–30 µm; 911 × 911 µm field of view; 1,024 × 1,024 pixel resolution). For higher magnification images, 20× 0.7 NA and 63× 1.4 NA oil objectives were used for SN neurons (similar parameters as above but with a 456 × 456 µm field of view) and dorsolateral striatum axonal profiles (stacks of *z* sections taken every 100 nm in a volume of ~2 µm; 49 × 49 µm field of view; 1024 × 1024 pixels), respectively, which were subsequently used for quantification. Colocalization between GCaMP3 and TH in SN cell bodies and dorsostriatal axonal structures was determined on single z-sections essentially as previously described[13] using Volocity's 'Measure Object Colocalization' task. A colocalization coefficient of 0.5 or higher was considered to be indicative of colocalization. Intensity threshold and size parameters were adjusted for the size and signal to noise ratio of the structures analyzed.

High K^+- and electrical stimulation–induced FFN destaining in brain slices. FFN200 and FFN102 release in response to K^+ depolarization or local electrical stimulation was monitored by time-lapse imaging on a Prairie Ultima Multiphoton Microscope (see above) with some modifications from the methods described previously[13]. FFN-labeled slices were imaged using excitation wavelengths of 740–770 nm and an emission range of 440–500 nm. To compensate for shifts in the z plane, z-stacks comprised of five 12-bit images acquired every 0.5 µm were continuously acquired over time and z sections representing the same field of view were selected for all time points for quantification. Image acquisition was performed averaging four frames of 22.5 × 22.5 µm and 256 × 256 pixels using a dwell time/pixel of 4.4 µs. This resulted in a time frame of 10–11s/z-stack. High K^+-induced destaining of FFN200 was performed by switching the perfusion solution to ACSF containing 40 mM KCl (prepared by isotonic replacement of NaCl), for at least 90 s, using a Rheodyne 7010 switching valve (Rheodyne/IDEX). For electrical stimulation experiments, the AMPA and NMDA receptor inhibitors NBQX (10 µM) and AP-5 (50 µM), respectively, were present in the perfused ACSF for 10 min before the onset of imaging and throughout the remainder of the experiment to prevent glutamatergic excitotoxicity. Slices were imaged for 35 time points and local electrical stimulation was applied from the beginning of time point 21 to the end of the recording. Stimulation pulses (each pulse 600 µs × 100 µA; number of pulses: 16, 160, 640 and 2,400, at 0.1, 1, 4 and 15 Hz, respectively) were applied locally to the dorsal striatum by an Iso-Flex stimulus isolator triggered by a Master-8 pulse generator (AMPI), using platinum bipolar electrodes (Plastics One). All images were acquired within 50–100 µm of one of the stimulating electrode poles. For Cd^{2+} and TTX experiments, 200 µM $CdCl_2$ or 1 µM TTX were present for 20 min before imaging and throughout the experiment. For 0 mM Ca^{2+} experiments, perfusion was switched to ACSF containing 2.4 mM $MgCl_2$ instead of $CaCl_2$ and 1 mM EGTA, 10 min before imaging onset. For the imaging of GCaMP3 and FFN200 destaining, slices were imaged essentially as above with the following exceptions. Images were continuously acquired in two channels with an interlaced sequential line scanning pattern using different imaging parameters for the two probes: FFN200 was excited at 770 nm and detected at an emission range of 435–485 nm and GCaMP3 was excited at 900 nm

and detected at 500–550 nm. Four frames of 19 × 19 µm and 180 × 180 pixels were averaged for each acquired image using a dwell time/pixel of 6.0 µs. Electrical stimulation was performed as above. After a short resting period, a 100 s pulse of 40 mM KCl was applied. Since Ca^{2+} signals in response to individual action potentials can be resolved by GCaMP3 monitoring at rates up to 6 Hz (ref. 55), 15 Hz trains were expected to elicit a sustained plateau-like increase in GCaMP3 intensity, amenable for detection with our image acquisition rate.

FFN image analysis. *Quantification of brain slice FFN200 puncta number and intensity.* FFN200 images and those used for the calculation of FFN200 puncta density were analyzed using Volocity 4.4 (Improvision/PerkinElmer) as described previously[13]. Briefly, fluorescent puncta were identified by defining a threshold of intensity as well as size and shape constraints. Similar analysis parameters were applied to conditions that were directly compared. After an automatic selection by the program, regions of interest (ROIs) that did not conform to a certain number of properties (for example, appropriate size and well-delimited boundaries) were manually discarded. Background fluorescence intensity was determined as the mean fluorescence intensity of areas of the image that excluded puncta. The mean background-subtracted fluorescent puncta intensity was then calculated by subtracting the mean background intensity from the mean fluorescence intensity measured at the puncta. For the calculation of FFN200 puncta density, we determined the size of the optical slice in z as the full-width half maximum of the squared illumination point spread function[56]. That value was 1.35 µm for an excitation wavelength of 750 nm and objective NA of 0.9. We then calculated the volume of a z-stack of five z-sections of 37.5 × 37.5 µm taken 0.5 µm apart to be 4.71×10^3 µm^3 and quantified the number of FFN200 puncta present in a maximal projection of the image z-stack as described above.

Quantification of brain slice FFN200-GFP colocalization. Colocalization between FFN200 fluorescent puncta and GFP was determined using Volocity's 'Measure Object Colocalization' task as described above for GCaMP3 and TH colocalization analysis. Visual inspection of each 'object' or ROI was performed to rule out obvious false positives and false negatives.

Cell culture FFN200 puncta analysis. To determine the percentage of dopamine neurons in mouse TH-GFP midbrain cultures that accumulated FFN200, GFP-positive neurons were considered FFN200-positive when their fluorescence intensity was greater than 2 s.d. above the mean FFN200 intensity of GFP-negative cells. For FFN200-synaptophysin colocalization analysis, FFN200 images were thresholded and ROIs were created for FFN200 fluorescent puncta using MetaMorph software (Molecular Devices). These ROIs were then applied to the corresponding synaptophysin images and the average synaptophysin fluorescence intensity was determined for each ROI. ROIs with a mean intensity value of at least 2 s.d. above the background were considered positive and the percentage of synaptophysin-positive FFN200 ROIs was calculated. Cultures were also stained for TH to confirm that analysis was performed exclusively on dopaminergic axons. FFN200-calbindin colocalization analysis of cell body images was performed in a similar manner as described for FFN200-synaptophysin colocalization, using the AxioVision software (Carl Zeiss Microscopy).

Quantification of KCl-induced FFN200 destaining. For brain slice experiments, MacBiophotonics ImageJ (NIH) was used to analyze KCl-induced FFN200 destaining. As KCl produces extensive xy and z shifts and distortion within the slice, we measured FFN200 fluorescence increase in the background, which was less prone to artifacts than puncta analysis. An in-house written macro was used to correct for shifts in the z dimension by selecting z sections representing the same field of view for all time points. Registration in xy was achieved using the 'PoorMan3Dreg' plugin (written by M. Liebling, a modification of Philippe Thévenaz's plugin StackReg). The mean background intensity of registered images was then calculated using ImageJ's 'rolling ball' method (Process/Subtract background/Create background). For cell culture experiments, acquired time-lapse images were corrected for xy shift in ImageJ using the 'PoorMan3DReg' plugin mentioned above. The first image of the time course was thresholded by eye and the resulting ROIs, corresponding to puncta between 0.4 and 16 µm^2 in size, were used to determine puncta intensities at all time points using MetaMorph software. The average puncta intensity for each time point was corrected for bleaching measured at 3–4 regions of FFN200-positive neurites that contained no punctate structures. Background fluorescence intensity, as measured in three areas devoid of cells, was subtracted from all values. For the plot shown in **Figure 3d**, only puncta destaining more than 20% were included.

Quantification of FFN200 and FFN102 destaining evoked by electrical stimulation. Image series were analyzed by custom-written Matlab software. Briefly, this routine registers image sets in xy and z dimensions, calculates and subtracts the background at each time point, and corrects individual puncta intensity versus time plots to remove the baseline rundown component throughout the trace. Puncta are then classified as destaining if they conform to two criteria described below. To correct for movement in the z-plane, an algorithm was written to identify a conserved subset of images at each time point. This algorithm measured the normalized two-dimensional cross-correlation in frequency space of every image to each image of the stack collected at the first time point, creating a plot of the movement of the image information present in each z section. A subset of images that were well-correlated were next registered in xy using a subpixel fast Fourier transform algorithm. The images at each time point were then averaged to reduce noise with no appreciable loss of signal. Each image was then thresholded using a multiple thresholding method to incrementally form ROIs over puncta without requiring a minimum brightness intensity. To account for stochastic movements made by puncta in the xy dimension during the imaging experiment, the ROIs were enlarged using a seeded watershed transform method in which the seeds were the centers of the puncta and the basin of the watershed an area around the puncta equivalent to a circle with a diameter equal to the median of the interpunctal distance. Puncta that appeared in the initial images but then disappeared before stimulation were automatically discarded using an algorithm that correlated ROIs at the different time points to each other. Any ROI that was not generated at both time points 1 and 20 was discarded. Image intensities were then collected for all ROIs and processed to subtract the background fluorescence and correct for baseline rundown. The background was measured by calculating the image intensities outside of the ROIs. We characterized this background increase as isotropic, permitting the subtraction of an average background intensity from the intensities of each punctum. The background-subtracted intensity for each ROI was normalized to the time point before stimulation. We then corrected the intensity plots to eliminate the contribution of the baseline rundown of FFN intensity, which showed a puncta-specific set of kinetics. The baseline rundown was determined for each punctum individually by fitting the baseline intensity values to an exponential decay function. To obtain the baseline-corrected intensities, the background-subtracted, normalized intensities of each punctum were divided by the baseline exponential fit for that punctum. This division was carried out over the domain of time points from the beginning of the image series to the first inflection point of the empirical function: puncta intensity – exponential fit intensity. Puncta were then classified as non-destaining or destaining, using a combination of principal component analysis and outlier analysis. For the principal component analysis, a matrix of all intensity over time data for all puncta was created. The principal components of this matrix were calculated using Matlab. Because the primary source of variability for the puncta was a result of the destaining at the point of stimulation, the puncta were then sorted into two groups, based on their weighting in the first principal component, using k-means clustering in order to minimize the total variance of weightings within each cluster. For the outlier analysis, a z-score was calculated for each intensity value after the stimulation begins using the mean and the s.d. of the baseline intensity values. To be considered as a destaining punctum, a z-score inferior to −2 s.d. of the mean baseline intensity was required in at least 10 out of the 15 time points during which stimulation was being applied. Only those puncta categorized as destaining by both principal component and the outlier methods were considered to destain and all remaining puncta were considered non-destaining. The intensity versus time plots of destaining puncta were then analyzed using GraphPad Prism 5 (GraphPad Software) to obtain the halftimes of destaining ($t_{1/2s}$) by fitting data with a monoexponential decay function. Puncta whose fit was determined as ambiguous or interrupted by the software and those with $t_{1/2}$ values determined to be extreme outliers for each condition (extreme outliers defined as $t_{1/2}$ values superior to 75% percentile + 3 × [25–75% interquartile range]) were discarded and were not included in the analysis. Due to experimental variability in the fraction of FFN destaining puncta and $t_{1/2}$ of destaining, conditions that were directly compared were performed on the same day, or if not possible, the same week.

Quantification of GCaMP3 signals evoked by electrical stimulation. The average GCaMP3 intensity corresponding to each FFN200 puncta ROI was determined using Matlab for GCaMP3 image series registered using the x, y and z registration information determined by the software for the matching FFN200 images.

doi:10.1038/nn.4252

To identify FFN200 puncta exhibiting a significant increase in GCaMP3 intensity in response to 15-Hz trains, the number of time points during the stimulation period that displayed GCaMP3 intensity values at least two s.d. above the mean baseline intensity were calculated for each puncta. A minimum of four stimulation time points with GCaMP3 intensities above the threshold was determined as a valid criterion to classify FFN200 puncta as exhibiting a GCaMP3 response to 15-Hz stimulation.

Code availability. An ImageJ macro to correct for shifts in the z dimension and the Matlab script for fluorescent puncta destaining analysis is available from our laboratory's website at http://sulzerlab.org/.

Imaging and analysis of FFN102 and FM1-43 colocalization. Striatal slices were incubated in the QE-1 imaging chamber with 10 µM FM1-43 in ACSF for 15 min in the presence of 50 µM AP-5 and 10 µM NBQX, under continuous oxygenation but without perfusion. FM1-43 loading was then performed in the same solution by local stimulation of the dorsal striatum with 3000 pulses at 15 Hz (each pulse 600 µs × 250 µA), as described above for FFN200 destaining but using stainless steel bipolar electrodes (Plastics One). Slices were then perfused at 6 ml min^{-1} with ACSF for 2 min followed by ACSF containing 100 µM ADVASEP-7 for 20 min, to maximize removal of extracellular FM1-43. After another 2 min of ACSF wash, perfusion was halted and slices were incubated in the imaging chamber with ACSF containing 15 µM FFN102 for 10 min. ACSF perfusion was resumed at 2 ml min^{-1} and imaging started 10 min later. Simultaneous z-stacks (5 z-sections taken 0.5 µm apart) of FFN102 and FM1-43 were acquired in two channels with a Prairie Ultima Multiphoton Microscope using an excitation wavelength of 760 nm and emission band pass filters of 440–500 nm and 570–640 nm, respectively, averaging four frames of a 38 × 38 µm field of view at 512 × 512 pixel resolution. Although a weak FM1-43 signal was detectible with 760-nm excitation, switching to 875-nm excitation afforded optimal FM1-43 signal. A single *z* image taken at 875 nm was then registered in xy with the corresponding single z image of FM1-43 taken simultaneously with FFN102 at 760 nm, for colocalization with the FFN. Depolarization with 40 mM KCl was then used to identify the specific activity-dependent FM1-43 signal. FFN102 and FM1-43 fluorescent puncta were identified using Volocity 4.4, as described above for FFN200. Activity-dependent FM1-43 puncta disappear completely upon KCl stimulation enabling identification. Colocalization analysis was performed by visual examination of several z sections following high K^+ stimulation, as this stimulus tended to distort the tissue.

CV. CV recordings of endogenous dopamine release were performed as detailed elsewhere[57], with some modifications. Carbon fiber electrodes of 5 µm in diameter were placed in the dorsal striatum (close to corpus callosum) ~70 µm into the slice. A triangular voltage wave (−450 to +800 mV at 294 mV ms^{-1}) was applied to the electrode every 100 ms and the resulting current was detected with an Axopatch 200B amplifier (Axon Instruments) using a 10 kHz low-pass Bessel Filter setting and a sampling rate of 25 kHz. Data was digitized using the ITC-18 board (Instrutech) and recorded with IGOR Pro 5.03 software (WaveMetrics), using an in-house written acquisition procedure. Striatal slices, kept under constant perfusion (2 ml min^{-1}) with oxygenated ACSF, were stimulated with a bipolar stainless steel electrode placed ~150 µm from the recording electrode, using an Iso-Flex stimulus isolator triggered by a Master-8 pulse generator (AMPI). Five single pulses (prepulses; 1 ms × 40 µA) were applied every 2 min to achieve constant dopamine release and from then onwards slices were stimulated with single pulses every 5 min. In dTBZ-treated slices, the perfusion solution was switched to ACSF containing 5 µM dTBZ, 8 min and 20 s into the recording (time point zero). Data were analyzed using an in-house written procedure in IGOR Pro. Current in response to each pulse was normalized to the average current of the five prepulses and results are expressed as mean normalized current ± s.e.m. All recordings were performed at 30 °C.

Statistics. Data is presented as mean ± s.e.m. and standard parametric tests were used for statistical analysis. When two conditions were compared, two-tailed *t*-tests were used while one way ANOVA was used for comparisons of three or more conditions. Two way ANOVA was used to compare intensity versus time traces between two conditions. The statistical test used in each experiment is defined in the corresponding figure legend. Sample size was chosen based on studies using related methods and is similar to what is generally employed in the field. Normal distribution of the data analyzed by parametric tests was confirmed by the Kolmogorov-Smirnov test whenever possible or otherwise assumed to be normal without a formal test. Equal variance of data groups being compared by two-tailed *t*-test was confirmed using F test or assumed without formal testing for ANOVA comparisons. Data collection and analysis were not randomized or performed blind to the conditions of the experiments.

A **Supplementary Methods Checklist** is available.

51. Adam, Y., Edwards, R.H. & Schuldiner, S. Expression and function of the rat vesicular monoamine transporter 2. *Am. J. Physiol. Cell Physiol.* **294**, C1004–C1011 (2008).
52. Giros, B., Jaber, M., Jones, S.R., Wightman, R.M. & Caron, M.G. Hyperlocomotion and indifference to cocaine and amphetamine in mice lacking the dopamine transporter. *Nature* **379**, 606–612 (1996).
53. Mena, M.A. *et al.* Effects of wild-type and mutated copper/zinc superoxide dismutase on neuronal survival and L-DOPA-induced toxicity in postnatal midbrain culture. *J. Neurochem.* **69**, 21–33 (1997).
54. Wong, M.Y., Sulzer, D. & Bamford, N.S. Imaging presynaptic exocytosis in corticostriatal slices. *Methods Mol. Biol.* **793**, 363–376 (2011).
55. Tian, L. *et al.* Imaging neural activity in worms, flies and mice with improved GCaMP calcium indicators. *Nat. Methods* **6**, 875–881 (2009).
56. Zipfel, W.R., Williams, R.M. & Webb, W.W. Nonlinear magic: multiphoton microscopy in the biosciences. *Nat. Biotechnol.* **21**, 1369–1377 (2003).
57. Schmitz, Y., Schmauss, C. & Sulzer, D. Altered dopamine release and uptake kinetics in mice lacking D2 receptors. *J. Neurosci.* **22**, 8002–8009 (2002).